

Temporal evolution of electric transport properties of $\text{YBa}_2\text{Cu}_3\text{O}_{7-\delta}$ Josephson junctions produced by focused-helium-ion-beam irradiation

M. Karrer^D, K. Wurster, J. Linek, M. Meichsner, R. Kleiner, E. Goldobin, and D. Koelle^{ID*}

Physikalisches Institut, Center for Quantum Science (CQ) and LISA⁺, Eberhard Karls Universität Tübingen, Auf der Morgenstelle 14, Tübingen 72076, Germany



(Received 18 November 2023; accepted 18 January 2024; published 31 January 2024)

We examined the temporal evolution of Josephson and resistive barriers created by a 30-keV focused helium ion beam in microbridges of epitaxially grown single-crystal $\text{YBa}_2\text{Cu}_3\text{O}_{7-\delta}$ thin films. Repeated electric transport measurements at 4.2 K within 300 days after irradiation revealed an increase in the critical current density j_c for devices stored at room temperature under nitrogen atmosphere. This behavior can be described by a diffusion-based model of displaced chain oxygen moving back to original lattice sites, thus healing the barrier and partially restoring critical current. We find that $j_c \propto \exp(-\sqrt{t/\tau})$ with time t . The relaxation time τ increases exponentially with helium irradiation dose and can exceed several hundred days for high-quality Josephson junctions. To achieve higher diffusion rates and thus shorter relaxation times, we annealed some devices in different oxygen partial pressures, right after irradiation. Within a week, those junctions relaxed to a quasistable state, making this a feasible option to achieve temporal stability of device parameters.

DOI: [10.1103/PhysRevApplied.21.014065](https://doi.org/10.1103/PhysRevApplied.21.014065)

I. INTRODUCTION

The manufacturing of superconducting electronics devices and circuits based on the high-transition temperature (high- T_c) cuprate superconductors is still challenging. Using a multilayer technology including trilayer Josephson junctions (JJs), difficulties arise due to complex material composition, the short superconductor coherence length and the need for fully epitaxial layer growth [1,2]. So far, high- T_c JJ technologies are vastly based on single-layer $\text{YBa}_2\text{Cu}_3\text{O}_{7-\delta}$ (YBCO) thin films with grain boundaries as Josephson barriers [3,4]. However, to rely on grain boundaries is heavily restricting with respect to possible circuit designs. In the 1990s, another approach was pursued with various attempts to create Josephson barriers in epitaxially grown YBCO films by local irradiation with high-energetic electron or ion beams [5–9]. However, the resulting barriers were lacking quality, e.g., in terms of lower values of the characteristic voltage V_c (critical current times junction resistance) and larger excess currents compared to grain-boundary-based JJs. After the invention of the gas-field ion source (GFIS) [10], which enabled unprecedentedly high spatial resolution in focused-ion-beam (FIB) imaging and patterning with 30-keV helium ions, a breakthrough in fabrication of JJs occurred [11]. Since then, the fabrication of JJs and more sophisticated devices by irradiating high- T_c

cuprate superconductors with a 30-keV focused He ion beam (He FIB) was reported by several groups [12–16].

The mechanism behind the fabrication of He-FIB-induced Josephson barriers in YBCO is, presumably as follows. The accelerated He ions with an energy of 30 keV have significant momentum compared to electrons and are capable of displacing the atoms in the YBCO lattice. SRIM [17] simulations show that mainly the chain oxygen, with approximately 1-eV binding energy [18] is displaced, which creates oxygen vacancies in YBCO [19]. Since superconductivity in YBCO heavily depends on the oxygen doping, one can expect a local reduction of the superconducting properties [20–22]. Therefore, He-FIB irradiation introduces a local imbalance of doping, which reduces with time due to thermal diffusion of oxygen, which drives the system back towards a state of (quasi)equilibrium.

Obviously, the temporal evolution of the He-FIB-induced defect structure at the barrier directly affects the electronic characteristics of the devices, i.e., device properties changes with time. This effect is certainly detrimental to applications where stable device properties are required. It has been shown already that devices can be stabilized by annealing after irradiation. So far, annealing of devices in YBCO was performed for devices produced by irradiation with (80–120)-keV electrons with a scanning-transmission-electron microscope [6] and 175-keV Ne^+ ions using a trilayer implantation mask [23]. However, the temporal evolution of parameters describing the electrical

*koelle@uni-tuebingen.de

transport properties of YBCO JJs produced by He-FIB irradiation has not yet been investigated, while research of the temporal stability of ion-irradiated junctions using nanolithography has already been reported [24,25]. Temporal stability is useful not only for applications where stable device parameters are needed over time but also for research, e.g., in concurrent measurements that need some time to setup. An easy known way for achieving temporal stability of He-FIB JJs is to store them at cryogenic temperatures. However, this method is under most circumstances not very suitable.

In this paper, we present the results obtained with a different approach: we first investigated the temporal evolution of electric transport parameters of He-FIB JJs, which were stored at room temperature in a nitrogen (N_2) atmosphere. Subsequently, we investigated how an annealing process with different oxygen (O_2) partial pressures changes the junction properties and their temporal evolution.

II. SAMPLE FABRICATION

We fabricated epitaxially grown *c*-axis-oriented YBCO thin films on $10 \times 10 \text{ mm}^2$ single-crystal (100) (LaAlO_3)_{0.3} ($\text{Sr}_2\text{AlTaO}_6$)_{0.7} (LSAT) substrates by pulsed-laser deposition (PLD) with a 20-nm-thick *in situ* Au layer on top deposited by electron-beam evaporation. For this study we used two chips (1 and 2), which were fabricated with nominally the same process parameters. To estimate the quality of the unpatterned YBCO films, x-ray diffraction (XRD) was performed after film growth, and the critical temperature T_c was measured using an inductive method [26].

Figure 1 shows a representative set of XRD measurements from chip 2. From the positions of the (00ℓ) Bragg peaks along the 2θ axis, the *c*-axis lattice constant of the YBCO film was determined to be 11.67 \AA . A YBCO film thickness $d = 30 \text{ nm}$ could be extracted from the Laue fringes [27] at the YBCO (001) Bragg peak (see left inset in Fig. 1). The right inset in Fig. 1 shows the rocking curve of the YBCO (005) Bragg peak. The full width at half maximum (FWHM) of the rocking curve is 0.069° , thus indicating a high crystal quality. Our films yield $T_c \approx 89 \text{ K}$, with a transition width below 1 K. Both YBCO films showed variations of their properties (T_c , thickness, FWHM of the rocking curve and *c*-axis lattice constant) below 5% of the given values.

For a two-step photolithography process we used a MLA100 MASKLESS ALIGNER (Heidelberg Instruments) and positive resist MA-P 1205 (Micro Resist Technology). During the first step we patterned the Au/YBCO bilayer by Ar ion milling to create microbridges with width $w = 3 \mu\text{m}$ and contact pads covered by Au. During the second step we removed the Au layer with commercially available Lugol's iodine TECHNIETCH™ ACI2 only on top of the

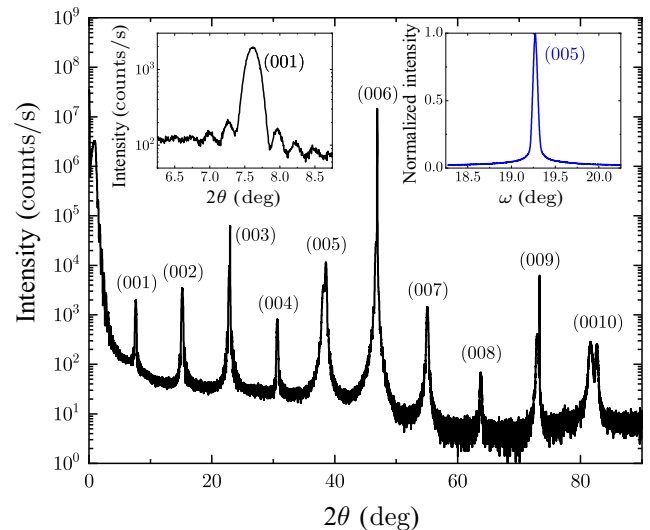


FIG. 1. XRD data of the unpatterned chip 2. Main graph: 2θ - ω overview scan with (00ℓ) Bragg peaks. Left inset: enlargement of the YBCO (001) peak with Laue fringes. Right inset: ω scan (rocking curve) at the YBCO (005) peak.

microbridges to expose the YBCO underneath, and along narrow stripes across the contact pads to split the Au contacts into two parts, enabling four-point measurements of the junctions later on. On each chip, we fabricated eight structures (A to H), each of which contain seven microbridges (each $50 \mu\text{m}$ long) in a meandering configuration. Figure 2 shows an optical microscope image after lithography of the central part of chip 2, structure A, denoted as 2A.

For He-FIB irradiation, the samples were mounted (and electrically grounded) on an aluminum sample stub and loaded into a ORION NANOFAB (Zeiss Microscopy). Junctions with different line dose D were written by irradiating with a 30-keV He FIB along a line perpendicular

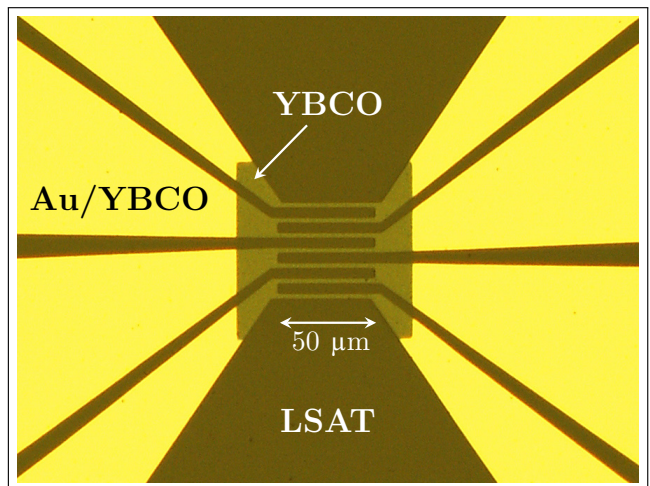


FIG. 2. Optical microscope image of the central part of structure 2A with seven microbridges after prepatternning.

to the YBCO microbridges. The beam current for fixed parameters of the ion focusing unit, e.g., spot size and aperture, resulted in 325 fA for 1A, 300 fA for 2D, and 200 fA for 2E. The dwell time per pixel was set to 1 μ s and the number of line repeats was varied to set different dose values in units of ions per nm, which are directly proportional to the beam current and automatically set for the deflection unit by the used NanoPatterning and Visualization Engine (NPVE). For typical beam currents of around 300 fA, the used doses from 100 to 1000 ions/nm require about 10 to 100 repeats, respectively. Within each structure, we denote the seven junctions by the different line doses used for He-FIB irradiation; for example, the junction on chip 1 located in structure A and irradiated with $D = 300$ ions/nm is denoted as 1A-300.

III. EXPERIMENTAL SETUP AND PROCEDURE

We measured current-voltage (I - V) characteristics and the modulation of the critical current I_c in an externally applied magnetic field B (along the normal to the YBCO film plane) in a current bias mode. For the $I_c(B)$ measurements a voltage criterion of 3 μ V was used to determine I_c . This criterion was 1 μ V above the typical noise level in our setup for the used gain settings of the preamplifiers. Measurements were performed by immersing the samples in liquid helium at temperature $T = 4.2$ K inside an electrically and magnetically shielded environment within a high-frequency shielding chamber.

In order to investigate the evolution of the properties of the junctions over time, we define day zero ($t = 0$) as the day when the bridges have been He-FIB-irradiated to form the JJs. Due to inevitable delays in the handling of the sample, the first measurement after the irradiation is conducted at $0 < t_{\text{initial}} \leq 1$ day. Furthermore, for the compensation of errors on the time axis we tracked (and subtracted) the time when the sample was in the measurement setup and exposed to lower temperatures.

A. Temporal evolution of the properties of junctions stored at room temperature

Chip 1 was stored in a flow box under N_2 atmosphere between measurements to avoid degradation of the YBCO surface due to air humidity [28]. Subsequently, and repeatedly, the JJ properties have been measured. In the beginning, measurements were performed more frequently for a better resolution of the larger rate of change of JJ properties right after irradiation.

B. Annealing at elevated temperatures

To stabilize the JJ properties, we annealed samples for a certain time t_a in an oxygen partial pressure p_{O_2} . Annealing was performed in a vacuum (annealing) chamber with inlets for O_2 and N_2 , with the sample placed on a resistive

heating element with an integrated temperature sensor. A digital temperature controller OMRON E5AC was used to set and keep the sensor temperature T_a constant during annealing. After sample loading, the annealing chamber was evacuated to an absolute pressure <0.1 mbar, then flooded with oxygen and evacuated to <0.1 mbar again to flush the chamber and the pipes from the gas bottle to the annealing system. After this procedure, p_{O_2} was set to the desired value and the temperature was ramped up to $T_a = 90$ °C with a rate of 20 °C/min. Pristine YBCO remains unharmed at 90 °C with no degradation even in vacuum [29].

After writing barriers into structure 2D, the chip 2 was annealed at $p_{O_2} = 950$ mbar for $t_a = 30$ min before the annealing chamber was flooded with O_2 to ambient pressure. Subsequently, the sample was placed onto a stainless steel plate for cooldown, outside the chamber in air. After completing measurements on structure 2D we wrote barriers into structure 2E and annealed chip 2 in vacuum. For this we just left the vacuum pump of the annealing chamber connected after the flushing procedure, i.e., during the subsequent annealing process for $t_a = 30$ min we had $p_{O_2} < 0.1$ mbar. Subsequently, we switched off the heater, vented the chamber with N_2 and then placed the sample onto a stainless steel plate for cooldown, outside the chamber in air.

Samples were measured directly after irradiation (at $t = 0$), have been annealed with the corresponding oxygen partial pressure at $t = 1$ day and measured subsequently all within 2 days. After this, the chip was stored under N_2 environment at room temperature and the junctions were repeatedly measured.

C. Evaluation of I - V characteristics

For junctions irradiated with $D \gtrsim 800$ ions/nm, i.e., close to the transition from medium to high dose (where amorphization sets in) [13], the I - V characteristics exhibit a $I \sim V^3$ contribution, in addition to a linear scaling $I \sim V$ (see Fig. 3), while for junctions with $D < 500$ ions/nm I - V characteristics exhibit an excess current I_{ex} . In order to consistently determine the normal state resistance R_n for all junctions, we applied an external magnetic field to suppress the critical current I_c and used the functional dependence

$$I(V) = aV^3 + \frac{V}{R_n} + \text{sgn}(V)I_{\text{ex}} \quad (1)$$

to fit all our measured I - V characteristics. Since I_c was never fully suppressed to zero, we discarded parts of the I - V characteristics where $|V| \leq 1$ mV for the evaluation of R_n . Here, the 1-mV criterion was used, as this was the typical voltage level, above which the I - V characteristics did coincide for any value of applied external magnetic field.

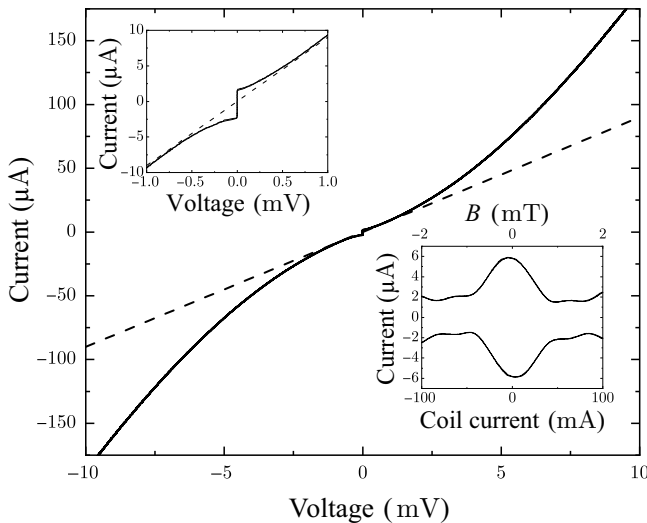


FIG. 3. I - V characteristics of junction 1A-1000 taken at the first minimum ($B \approx 0.94$ mT) of $I_c(B)$ after $t = 160$ days clearly bending away from an Ohmic resistance (dashed line) for larger voltages. The upper left inset shows an enlargement of the I - V characteristics at smaller voltages and currents. The lower right inset shows a measurement of $I_c(B)$. The bottom axis refers to the applied coil current and the top axis is the calculated magnetic field from the experimentally determined coil constant by using a Hall probe.

The maximum critical current $I_{c,\max}$ for each junction was determined from the maximum of the recorded $I_c(B)$ curves. Note that due to thermal noise rounding, the experimentally determined $I_{c,\max}$ can be significantly suppressed below the noise-free maximum critical current I_0 . From numerical simulations of overdamped JJs within the resistively and capacitively shunted junction (RCSJ) model, one knows that for a noise parameter $\Gamma \equiv I_{\text{th}}/I_0 = 0.05$, with $I_{\text{th}} = 2\pi k_B T/\Phi_0$, $I_{c,\max}$ of a nonhysteretic junction is suppressed by approximately 10% (Φ_0 is the magnetic flux quantum and k_B is the Boltzmann constant) [30]. With $I_{\text{th}} \approx 176$ nA at $T = 4.2$ K, a noise parameter $\Gamma = 0.05$ corresponds to $I_0 \approx 3.5$ μ A, i.e., significant noise rounding is only expected for JJs with critical currents below a few μ A, which is only relevant for the junction 1A-1000, for which the measured $I_{c,\max}$ is a lower bound.

IV. RESULTS AND DISCUSSION

Now we discuss and analyze the evolution of the electric transport properties of He-FIB JJs with time. Note that unless stated otherwise, for simplicity, we denote now the maximum (with respect to variable magnetic field B) critical current as I_c and the corresponding maximum critical current density as $j_c = I_c/(wd)$.

A. Temporal evolution of electric transport properties of He-FIB JJs stored at room temperature

Here, we present results on He-FIB JJs, which were stored at room temperature. Figure 4 shows the time

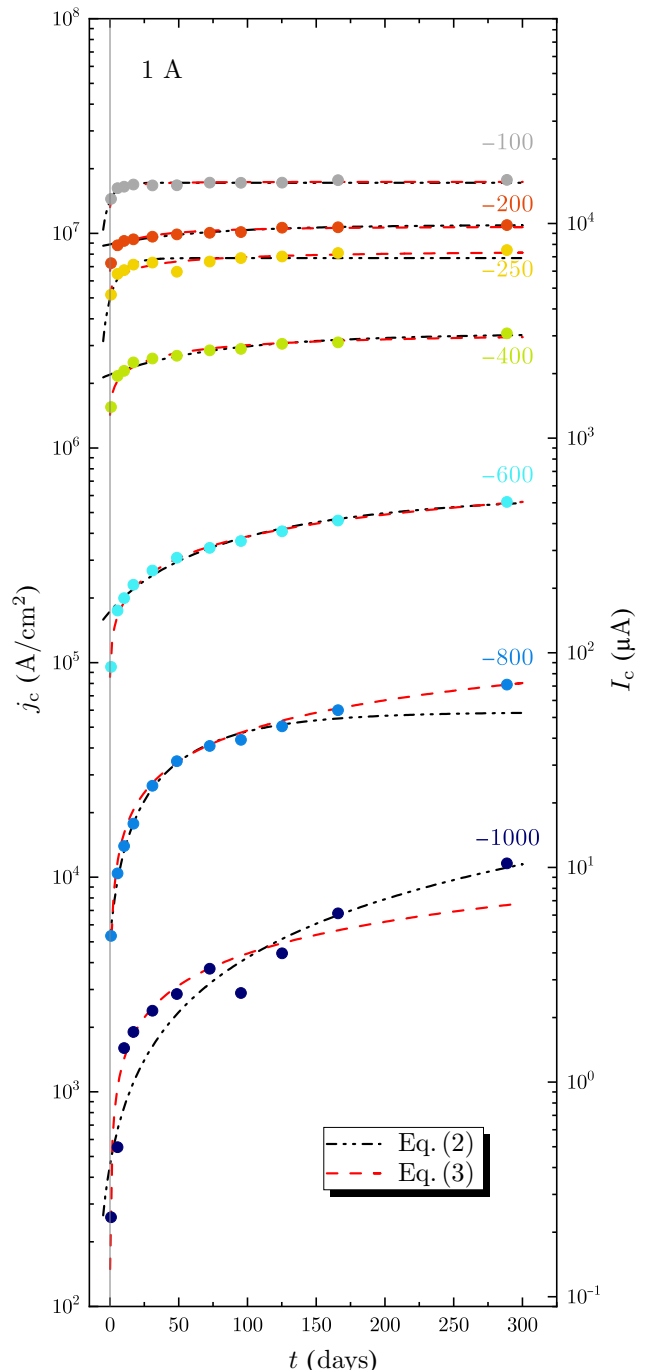


FIG. 4. Time dependence of the critical current density $j_c(t)$ (left axis: j_c in A/cm^2) and critical current I_c (right axis: I_c in μA) for junctions from 1A-100 to 1A-1000 and stored at room temperature. The dash-dotted and dashed lines show fits to the experimental data (symbols), obtained from Eqs. (2) and (3), respectively.

dependence of the critical current density $j_c(t)$ of the seven JJs 1A-100 to 1A-1000 located in structure 1A over 160 days after irradiation. Obviously, j_c is largest for the JJ irradiated with the lowest dose $D = 100$ ions/nm (top curve in Fig. 4) and smallest for the JJ irradiated with the

highest dose $D = 1000$ ions/nm (bottom curve in Fig. 4). We find a monotonous increase in $j_c(t)$, which tends to saturate for long enough times. However, we also see a clear dose dependence in the evolution of $j_c(t)$. For the lowest dose (junction 1A-100), already after a few days j_c saturates. With increasing dose (junctions 1A-200 to 1A-400), the time until saturation of j_c is reached steadily increases, and for the highest doses (junctions 1A-600 to 1A-1000) $j_c(t)$ has not saturated at $t = 288$ days.

To fit the experimental data we used two different equations

$$j_c(t) = j_{c,\infty} \left[1 - b \exp\left(-\frac{t}{\tau}\right) \right]; \text{ and} \quad (2)$$

$$j_c(t) = j_{c,\infty} \left[1 - b \exp\left(-\sqrt{\frac{t}{\tau}}\right) \right]. \quad (3)$$

Here $j_{c,\infty}$ is the saturation (equilibrium) value of the critical current, which is achieved for $t \rightarrow \infty$. This parameter can be associated with unrecoverable damage in the barrier region induced by He-FIB irradiation. The dimensionless parameter $b = (j_{c,\infty} - j_{c,0})/j_{c,\infty}$ [with $j_{c,0} \equiv j_c(t=0)$] describes the degree of nonequilibrium damage that was created by He-FIB irradiation and which can still be recovered with time (by annealing). $b = 0$ means that we are at equilibrium already at $t = 0$ and there is nothing to recover. $b = 1$ means that the He-FIB irradiation initially completely suppresses the critical current density, i.e., $j_{c,0} = 0$, but with time finite j_c will appear. The parameter τ describes the characteristic time scale (relaxation time) that governs relaxation of the system to the equilibrium state. The two formulas are similar, but Eq. (2) describes the changes in j_c due to a *constant flux* of oxygen atoms diffusing towards the barrier, while Eq. (3) describes the *diffusion* of a limited amount of oxygen atoms towards the barrier. Equation (2) assumes that the sample is placed in a oxygen atmosphere and the oxygen atoms diffuse into the barrier from the outside; instead Eq. (3) assumes that oxygen atoms that have been displaced during He-FIB irradiation diffuse back similar to Einstein diffusion. By using Eqs. (2) and (3) to fit the data shown in Fig. 4, we conclude that Eq. (3) allows to fit the experimental data more consistently at smaller times for devices irradiated with higher doses.

As a result of fitting with Eq. (3) we obtain the dose dependence of the fitting parameters $j_{c,\infty}$, b , and τ as shown in Fig. 5. For $j_{c,\infty}$ we find an exponential decay with increasing dose [see Fig. 5(a)], i.e.,

$$j_{c,\infty}(D) \approx j_{c,\infty}(0) \exp(-D/D_0), \quad (4)$$

with $j_{c,\infty}(0) = 3.2 \times 10^7$ A/cm² and $D_0 = 191$ ions/nm. The value for $j_{c,\infty}(0)$ corresponds to the critical current density of unirradiated YBCO films at 4.2 K; this

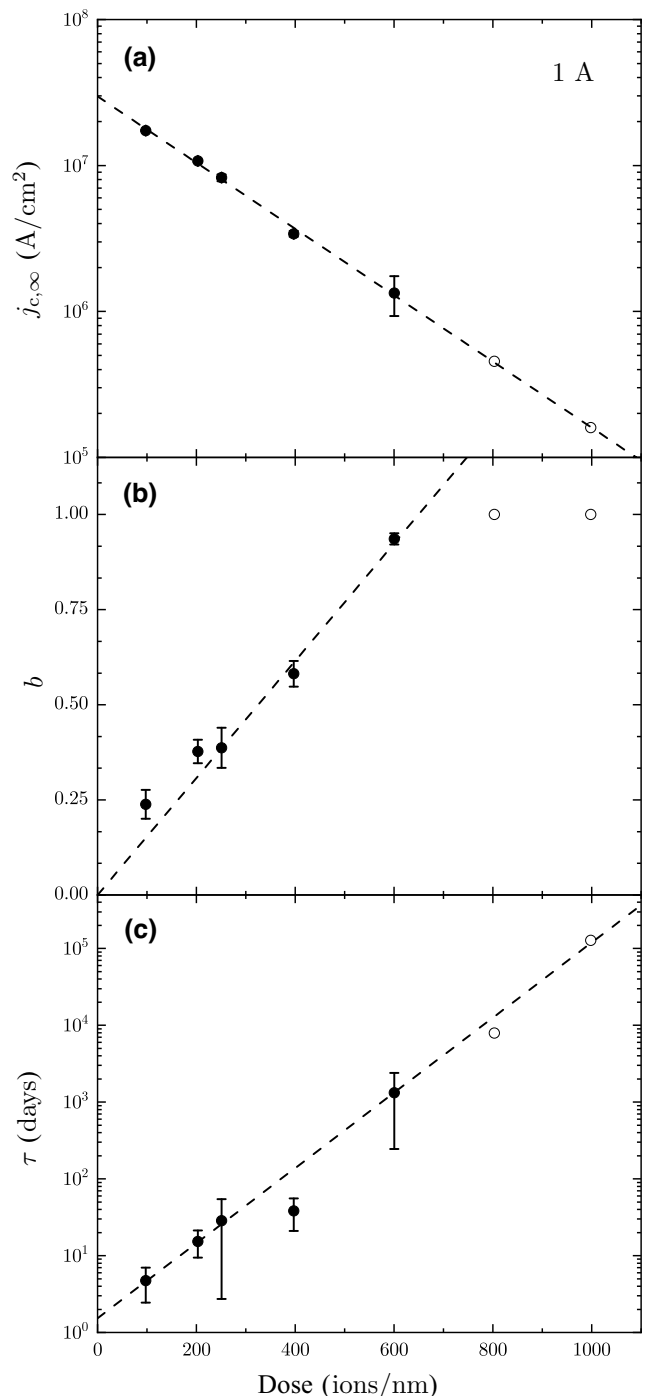


FIG. 5. Dose dependence of the parameters $j_{c,\infty}$ (a), b (b), and τ (c) extracted from the fits with Eq. (3) to $j_c(t)$ data shown in Fig. 4. For the two highest dose values, the $j_{c,\infty}$ values [open symbols in (a)] have been fixed for the fitting procedure to obtain b and τ [31]. The confidence intervals provided by the fitting algorithm are shown as error bars.

coincides quite well with the corresponding value given in Ref. [13]. The value for the characteristic dose D_0 obtained in the present study is slightly higher than the

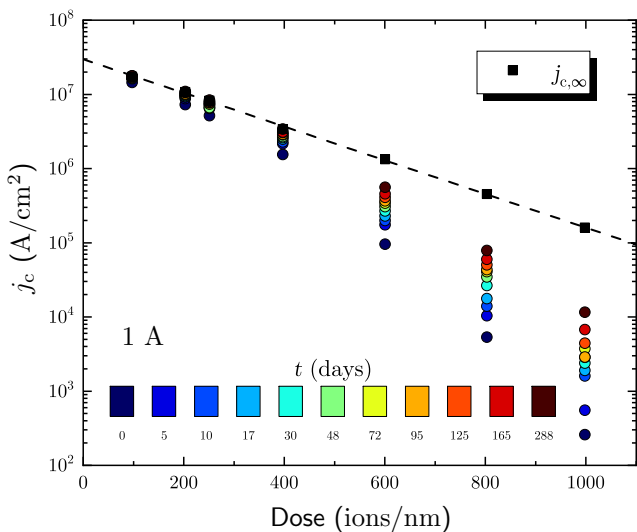


FIG. 6. Experimentally determined critical current density j_c versus irradiation dose D for junctions from 1A, measured at different times t after irradiation (indicated by the color scale). For comparison the fit parameter $j_{c,\infty}(D)$ is shown as black squares.

value $D_0 = 130$ ions/nm found for the exponential scaling of $j_c(D)$ (measured at some finite t) for YBCO He-FIB JJs on SrTiO₃ (STO) or MgO substrates and significantly higher than $D_0 = 38$ ions/nm found for YBCO He-FIB JJs on a LSAT substrate [13]. The reason for the low value of $D_0 = 38$ ions/nm on LSAT in Ref. [13] has not yet been clarified. We note that we observe the tendency that for our YBCO He-FIB JJs produced on the same chip (typically on LSAT substrates), we always find an exponential decay of $j_c(D)$ with a well-defined D_0 . However, the value of D_0 can vary significantly from chip to chip. Currently, it is not clear whether D_0 is related to and affected by the YBCO film quality or by the conditions in the helium ion microscope. What is obvious from the study presented here is the fact that D_0 is also affected by the time t (samples stored at room temperature) after He-FIB irradiation. This is illustrated in Fig. 6, which shows the same experimental data (dots) as in Fig. 4, but now plotted as $j_c(D)$ for different values of t , together with $j_{c,\infty}(D)$ (squares) from Fig. 5(a). Clearly, with increasing t the slope $|\partial \log j_c / \partial D|$ decreases, i.e., D_0 increases, approaching asymptotically the scaling of $j_{c,\infty}(D)$. Thus, experimentally measured $j_c(D)$ tends to decrease the slope with time and becomes more straight.

The scaling of $b(D)$, shown in Fig. 5(b), is approximately linear for $D \lesssim 600$ ions/nm and saturates to $b \approx 1$ for larger D . In the latter case, the permanent and nonequilibrium damage make $j_{c,0} = 0$. However, if one removes nonequilibrium damage by storing at room temperature, j_c recovers to some finite value, which is caused by permanent damage only.

Obviously, the characteristic time for recovery increases with D . This is illustrated in Fig. 5(c), which shows that

the time constant τ increases exponentially with dose and can be described by

$$\tau(D) \approx \tau_0 \exp(D/D_{0,\tau}), \quad (5)$$

with $\tau_0 = 1$ day and $D_{0,\tau} = 89$ ions/nm. Interestingly, the value of $D_{0,\tau}$ is not far from half of the value of D_0 . However, it is not clear whether or not this is just a coincidence. Still, it is worthwhile to note that for typical doses required to create RCSJ-like Josephson junctions without an excess current, i.e., $D \gtrsim 500$ ions/nm, the value of $\tau \gtrsim 100$ days. This means that the properties of junctions produced with such doses change over significant time scales of up to a year, if they are stored at room temperature.

In addition to $j_c(t)$ shown in Fig. 4, we also measured the time evolution $R_n(t)$ and calculated $\rho_n(t)$ (not shown). This allows us to calculate $V_c(t) = j_c(t)\rho_n(t)$ and its evolution during annealing, see Fig. 7. In Ref. [13] we showed that the exponential scaling of characteristic He-FIB JJ properties (j_c , $\rho_n = R_n w d$ and the characteristic voltage $V_c \equiv I_c R_n \equiv j_c \rho_n$) with D can be described by the same values of D_0 , indicating a universal scaling of V_c with either j_c or ρ_n , and we found an approximate scaling $V_c \approx V_{c,1} (j_c/j_{c,1})^{1/2}$. Now, for the He-FIB JJs described here, we find the same scaling $V_c \propto j_c^{1/2}$, as shown in Fig. 7. Note that this is not only true for the junctions measured directly after irradiation, but also for junctions stored at room temperature and remeasured over the whole time of the experiment (up to $t = 288$ days), i.e., for the same junction, the data points move with t along the $V_c \propto j_c^{1/2}$ line. The data points for the He-FIB JJs 1A-400, 1A-600, and 1A-800 follow the

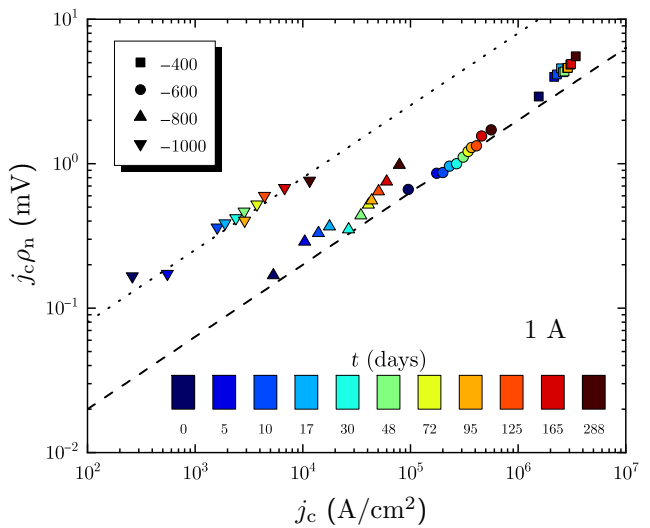


FIG. 7. $j_c \rho_n$ versus j_c for He-FIB JJs (from 1A) stored at room temperature and measured at different times t after irradiation (indicated by the color scale). The dashed and dotted lines represent $j_c \rho_n = V_{c,1} \sqrt{j_c / j_{c,1}}$, with $V_{c,1} = 2$ and 8 mV, respectively ($j_{c,1} = 10^6$ A/cm²).

same scaling with $V_{c,1} = 2$ mV and $j_{c,1} = 10^6$ A/cm² as reported in Ref. [13]. However the data points for junction 1A-1000 with $D = 1000$ ions/nm show a significant offset, i.e., they also show the scaling $V_c \propto j_c^{1/2}$, but now with a factor of 4 larger $V_{c,1} = 8$ mV and $j_{c,1} = 10^6$ A/cm². In conclusion, we observed an increase in the critical current density, respectively, a decrease in the resistivity, over time when devices were stored at room temperature. With our diffusion-based model, a reasonable explanation is, that oxygen atoms displaced during irradiation to interstitial lattice sites are diffusing back to their original position, healing the barrier and thus the critical current density increases.

B. Temporal evolution of electric transport properties of He-FIB JJs that were annealed after irradiation

The temporal evolution of the critical current density of He-FIB JJs from structure 2D is presented in Fig. 8. Those junctions have been annealed twice (at 90 °C) in oxygen ($p_{O_2} = 950$ mbar) for 30 min at day 1 and day 41 (j_c measurements on day 1 and 41 have been performed after annealing). Annealing the junctions at day 1 caused an increase in j_c and a decrease in ρ_n , respectively, just after the annealing step. After 1 week the critical currents were reduced, but still maintained higher values than obtained directly after irradiation. In the following weeks j_c did not change significantly, indicating that the junctions have reached a quasistable state. On day 41 we repeated the same annealing procedure with the already annealed junctions. The temporal evolution of j_c showed qualitatively the same behavior as after the first annealing step, however j_c values are higher and there seems to appear now a short

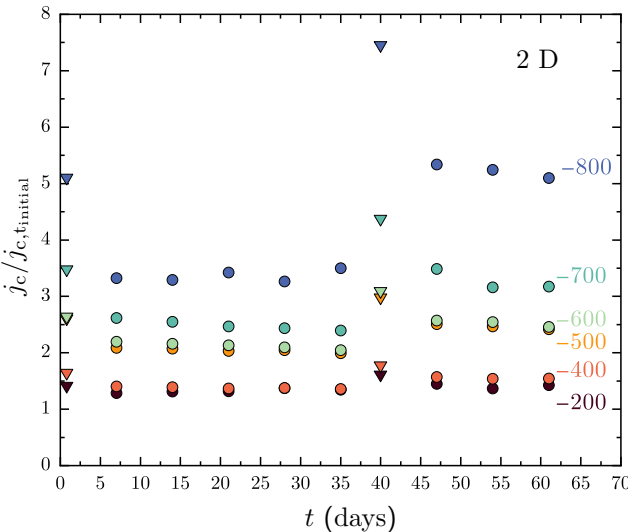


FIG. 8. Temporal evolution of the critical current density j_c (normalized to j_c at $t = t_{\text{initial}}$) of He-FIB JJs from 2D, which were annealed at 90 °C for 30 min in $p_{O_2} = 950$ mbar.

but finite relaxation time until another quasistable state has been reached.

In Fig. 9, the data from Fig. 8 are plotted against the dose D for substantial points in time, namely after irradiation ($t = t_{\text{initial}}$) and for both quasistable states after relaxation following the first and second annealing step ($t = 21$ and 61 days, respectively). We find, that with comparable initial critical current densities (right after He-FIB irradiation), the first annealing step increased j_c equivalently to roughly 100 days of storing at room temperature, while the second annealing step produced another increase in j_c , albeit at a moderate level. Moreover, the junctions after annealing do not exhibit a significant further change in j_c with time (cf. Fig. 8), which one would expect if following the time evolution shown in Fig. 4, but remained unchanged in their electric transport properties. This clearly indicates that moderate thermal annealing after He-FIB irradiation clearly stabilizes the irradiation-induced defect structure.

Similar to the graph in Fig. 7 the overall scaling $V_c(j_c)$ for the annealed junctions is shown in Fig. 10. As the junctions stored at room temperature, the annealed junctions follow the same $V_c \propto j_c^{1/2}$ scaling indicated by the dotted and dashed lines. In addition one can see that the higher-dose junctions are shifted towards higher characteristic voltages for the same critical current density.

For comparison, and to rule out the possibility that the increase in j_c shortly after annealing is caused by the high oxygen pressure in the annealing chamber during the

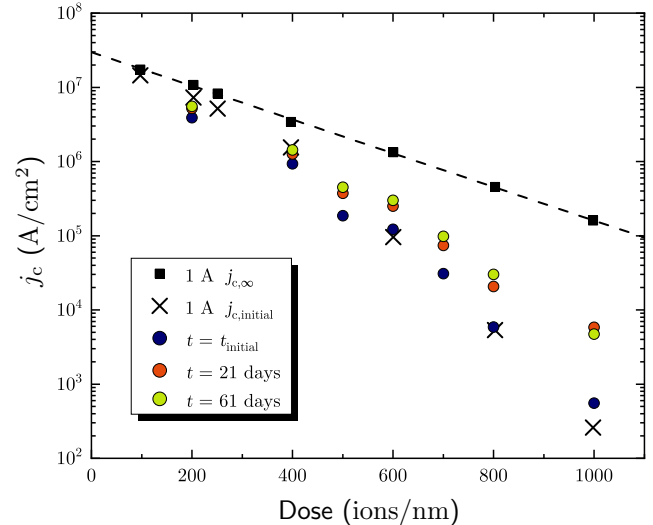


FIG. 9. Critical current density j_c versus irradiation dose D for He-FIB JJs from 2D (annealed at 90 °C for 30 min in $p_{O_2} = 950$ mbar), measured at substantial times ($t = t_{\text{initial}}$, 21 days and 61 days). For comparison, we show results from JJs from 1A—stored at room temperature—for the initial critical current density (black crosses) and $j_c,\infty(D)$ (dashed line and black squares).

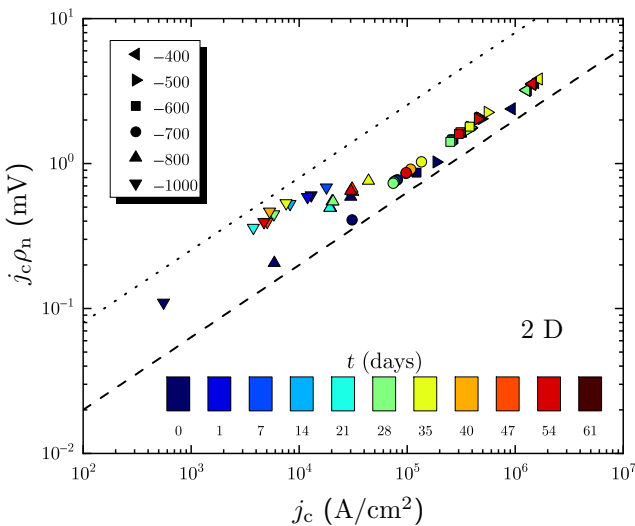


FIG. 10. $j_c \rho_n$ versus j_c for He-FIB JJs from 2D annealed at 90 °C for 30 min in $p_{O_2} = 950$ mbar. The dashed and dotted lines represent $j_c \rho_n = V_{c,1} \sqrt{j_c / j_{c,1}}$, with $V_{c,1} = 2$ and 8 mV, respectively ($j_{c,1} = 10^6$ A/cm 2).

treatment, we performed annealing of He-FIB JJs from structure 2E at $p_{O_2} < 0.1$ mbar. Here, we could not observe a substantial difference of the temporal evolution of j_c as compared to junctions annealed at $p_{O_2} = 950$ mbar. This observation indicates, that the restoring of critical current density with annealing (or also simply by storing at room temperature) is due to the diffusion of oxygen atoms that have been displaced (probably to interstitial sites) by He-FIB irradiation and that are diffusing back to lattice sites. Obviously, the annealing process significantly speeds up the relaxation (back diffusion) to a quasistable state with stable electric transport properties.

V. CONCLUSIONS

We fabricated Josephson barriers in prepatterned 3-μm-wide microbridges of epitaxially grown YBCO thin films by scanning a focused He ion beam across the bridges, which locally modifies the superconducting properties of the thin film. In detail, we studied the temporal evolution of characteristic junction properties for devices stored at room temperature and found that this process can be best described by a diffusion-based model, corresponding to a limited amount of oxygen diffusing back towards the barrier. Moreover, fitting of the experimentally observed temporal evolution of critical current density with time, allowed us to extract the dose dependence of the fitting parameters $j_{c,\infty}$, b and τ . For high-quality junctions, corresponding to doses in the range of 600–800 ions/nm, the relaxation time is typically $\tau \sim 100$ –1000 days, exceeding any feasible timescale to wait for the equilibrium state. The analysis of the characteristic voltages V_c of the fabricated

devices yield a scaling $V_c \propto \sqrt{j_c}$, also reported in previous work [13], but now this scaling holds true even for junctions stored at room temperature over the whole time of the experiment.

Furthermore, we examined the behavior of devices when treated with an annealing step at high oxygen pressures. Directly after the treatment the critical current density j_c increased before relaxing into a quasistable state within the first week. A repeated annealing step increased j_c only marginally, but indicated a slightly larger relaxation time of roughly 2 weeks. In comparison to junctions stored at room temperature, the annealing process accelerated the increase in j_c to roughly an equivalent of 100 days storing at room temperature. Additionally, for annealing at low oxygen pressures we did not observe any substantial differences in the behavior of the annealed devices annealed at high oxygen pressure. This indicates that predominantly the oxygen atoms displaced during He-FIB irradiation are diffusing back towards the original lattice sites.

Although some enigma remains to be examined in further studies, we revealed how characteristic properties of He-FIB JJs in YBCO evolve with time when stored at room temperature and confirmed a strategy to stabilize their properties. The stabilization of device parameters after annealing is expected to result in smaller spread (in particular, over time) and improved device uniformity. This in turn will significantly support the development of complex multijunction circuits (e.g., for digital applications) with different j_c (produced by different dose values) yielding e.g., better operation margins. So far, we have not systematically varied the annealing procedure, and there might still be room for improvements. In particular, one might implement an *in situ* annealing procedure with the He-FIB circuit fabrication process by utilizing the heating stage of the Orion NanoFab. We anticipate that such an *in situ* process might provide stable parameters immediately following the He-FIB irradiation, thus further increasing the feasibility of this technology.

ACKNOWLEDGMENTS

We gratefully acknowledge technical support by M. Turad, R. Löffler (LISA⁺), C. Back, and R. Schilling. This work was supported by the Deutsche Forschungsgemeinschaft (DFG) (GO 1106/6-1), by the European Commission under H2020 FET Open Grant “FIBsuperProbes” (Grant No. 892427) and by the COST actions FIT4NANO (CA19140) and SUPERQUMAP (CA21144).

-
- [1] D. Koelle, R. Kleiner, F. Ludwig, E. Dantsker, and J. Clarke, High-transition-temperature superconducting quantum interference devices, *Rev. Mod. Phys.* **71**, 631 (1999).

- [2] F. Ludwig, D. Koelle, E. Dantsker, D. Nemeth, A. Miklich, J. Clarke, and R. Thomson, Low noise $\text{YBa}_2\text{Cu}_3\text{O}_{7-x}$ - SrTiO_3 - $\text{YBa}_2\text{Cu}_3\text{O}_{7-x}$ multilayers for improved magnetometers, *Appl. Phys. Lett.* **66**, 373 (1995).
- [3] H. Hilgenkamp and J. Mannhart, Grain boundaries in high- T_c superconductors, *Rev. Mod. Phys.* **74**, 485 (2002).
- [4] R. Gross, L. Alff, A. Beck, O. Froehlich, D. Koelle, and A. Marx, Physics and technology of high temperature superconducting Josephson junctions, *IEEE Trans. Appl. Supercond.* **7**, 2929 (1997).
- [5] S. S. Tinchev, Investigation of RF SQUIDs made from epitaxial YBCO films, *Supercond. Sci. Technol.* **3**, 500 (1990).
- [6] S. K. Tolpygo, S. Shokhor, B. Nadgorny, J.-Y. Lin, M. Gurvitch, A. Bourdillon, S. Y. Hou, and J. M. Phillips, High quality $\text{YBa}_2\text{Cu}_3\text{O}_7$ Josephson junctions made by direct electron beam writing, *Appl. Phys. Lett.* **63**, 1696 (1993).
- [7] W. E. Booij, A. J. Pauza, E. J. Tarte, D. F. Moore, and M. G. Blamire, Proximity coupling in high- T_c Josephson junctions produced by focused electron beam irradiation, *Phys. Rev. B* **55**, 14600 (1997).
- [8] D.-J. Kang, G. Burnell, S. J. Lloyd, R. S. Speaks, N. H. Peng, C. Jeynes, R. Webb, J. H. Yun, S. H. Moon, B. Oh, E. J. Tarte, D. F. Moore, and M. G. Blamire, Realization and properties of $\text{YBa}_2\text{Cu}_3\text{O}_{7-\delta}$ Josephson junctions by metal masked ion damage technique, *Appl. Phys. Lett.* **80**, 814 (2002).
- [9] N. Bergeal, J. Lesueur, M. Sirena, G. Faini, M. Aprili, J. P. Contour, and B. Leridon, Using ion irradiation to make high- T_c Josephson junctions, *J. Appl. Phys.* **102**, 083903 (2007).
- [10] B. W. Ward, J. A. Notte, N. P. Economou, and Helium ion microscope, A new tool for nanoscale microscopy and metrology, *J. Vac. Sci. Technol. B: Microelectron. Nanometer Struct.* **24**, 2871 (2006).
- [11] S. A. Cybart, E. Y. Cho, J. T. Wong, B. H. Wehlin, M. K. Ma, C. Huynh, and R. C. Dynes, Nano Josephson superconducting tunnel junctions in $\text{YBa}_2\text{Cu}_3\text{O}_{7-\delta}$ directly patterned with a focused helium ion beam, *Nat. Nano* **10**, 598 (2015).
- [12] E. Y. Cho, Y. W. Zhou, J. Y. Cho, and S. A. Cybart, Superconducting nano Josephson junctions patterned with a focused helium ion beam, *Appl. Phys. Lett.* **113**, 022604 (2018).
- [13] B. Müller, M. Karrer, F. Limberger, M. Becker, B. Schröppel, C. J. Burkhardt, R. Kleiner, E. Goldobin, and D. Koelle, Josephson junctions and SQUIDs created by focused helium-ion-beam irradiation of $\text{YBa}_2\text{Cu}_3\text{O}_7$, *Phys. Rev. Appl.* **11**, 044082 (2019).
- [14] F. Couëdo, P. Amari, C. Feuillet-Palma, C. Ulysse, Y. K. Srivasta, R. Singh, N. Bergeal, and J. Leseur, Dynamic properties of high- T_c superconducting nano-junctions made with a focused helium ion beam, *Sci. Rep.* **10**, 021001 (2020).
- [15] Z. Chen, Y. Li, R. Zhu, J. Xu, D. Y. T. Xu, X. Cai, Y. Wang, J. Lu, Y. Zhang, and P. Ma, High-temperature superconducting $\text{YBa}_2\text{Cu}_3\text{O}_{7-\delta}$ Josephson junction fabricated with a focused helium ion beam, *Chin. Phys. Lett.* **39**, 077402 (2022).
- [16] R. L. Merino, P. Seifert, J. D. Retamal, R. K. Mech, T. Taniguchi, K. Watanabe, K. Kadokawa, R. H. Hadfield, and D. Efetov, Two-dimensional cuprate nanodetector with single telecom photon sensitivity at $T = 20$ K, *2D Mater.* **10**, 10256 (2023).
- [17] J. F. Ziegler, M. D. Ziegler, and J. P. Biersack, SRIM—the stopping power and range of ions in matter, *Instrum. Methods Phys. Res., Sect. B* **268**, 1818 (2010).
- [18] F. Z. Cui, J. Xie, and H. D. Li, Preferential radiation damage of the oxygen sublattice in $\text{YBa}_2\text{Cu}_3\text{O}_7$: A molecular-dynamics simulation, *Phys. Rev. B* **46**, 11182 (1992).
- [19] W. Lang, M. Marksteiner, M. A. Bodea, K. Siraj, J. D. Pedarnig, R. Kolarova, P. Bauer, K. Haselgrübler, C. Hasenfuss, I. Beinik, and C. Teichert, Ion beam irradiation of cuprate high-temperature superconductors: Systematic modification of the electrical properties and fabrication of nanopatterns, *Nucl. Instr. Meth. Phys. B* **272**, 300 (2012).
- [20] K. L. Mletschnig and W. Lang, Nano-patterning of cuprate superconductors by masked He^+ ion irradiation: 3-dimensional profiles of the local critical temperature, *Microelectron. Eng.* **215**, 110982 (2019).
- [21] B. Aichner, B. Müller, M. Karrer, V. R. Misko, F. Limberger, K. L. Mletschnig, M. Dosmailov, J. D. Pedarnig, F. Nori, R. Kleiner, D. Koelle, and W. Lang, Ultra-dense tailored vortex pinning arrays in superconducting $\text{YBa}_2\text{Cu}_3\text{O}_{7-\delta}$ thin films created by focused he ion beam irradiation for fluxonics applications, *ACS Appl. Nano Mater.* **2**, 5108 (2019).
- [22] B. Aichner, K. L. Mletschnig, B. Müller, M. Karrer, M. Dosmailov, J. D. Pedarnig, R. Kleiner, D. Koelle, and W. Lang, Angular magnetic-field dependence of vortex matching in pinning lattices fabricated by focused or masked helium ion beam irradiation of superconducting $\text{YBa}_2\text{Cu}_3\text{O}_{7-\delta}$ thin films, *Low Temp. Phys.* **46**, 331 (2020).
- [23] E. Y. Cho, K. Kouperine, Y. Zhuo, R. C. Dynes, and S. A. Cybart, The effects of annealing a 2-dimensional array of ion-irradiated Josephson junctions, *Supercond. Sci. Technol.* **29**, 094004 (2016).
- [24] A. Katz, S. Woods, R. Dynes, and A. Sun, Stability and uniformity of planar high temperature Josephson junctions fabricated using nanolithography and ion damage, *IEEE Trans. Appl. Supercond.* **9**, 3005 (1999).
- [25] S. A. Cybart, P. Roediger, K. Chen, J. M. Parker, E. Y. Cho, T. J. Wong, and R. C. Dynes, Temporal stability of $\text{Y}-\text{Ba}-\text{Cu}-\text{O}$ nano Josephson junctions from ion irradiation, *IEEE Trans. Appl. Supercond.* **23**, 1100103 (2013).
- [26] H. Hochmuth and M. Lorenz, Inductive determination of the critical current density of superconducting thin films without lateral structuring, *Physica C* **220**, 209 (1994).
- [27] A. M. Miller, M. Lemon, M. A. Choffel, S. R. Rich, F. Harvel, and D. C. Johnson, Extracting information from x-ray diffraction patterns containing Laue oscillations, *Z. Naturforsch. B* **77**, 313 (2022).
- [28] M. W. Hooker, S. A. Wise, I. A. Carlberg, R. M. Stephens, R. T. Simchick, and A. Farjam, Room temperature degradation of $\text{YBa}_2\text{Cu}_3\text{O}_{7-x}$ superconductors in varying relative humidity environments, Technical Paper number 3368 (NASA, 1993).
- [29] A. Mogro-Campero, K. W. Paik, and L. G. Turner, Degradation of thin films of $\text{YBa}_2\text{Cu}_3\text{O}_7$ by annealing in air and in vacuum, *J. Supercond.* **8**, 95 (1995).
- [30] B. Chesca, R. Kleiner, and D. Koelle, in *The SQUID Handbook*, Vol. 1, Fundamentals and Technology of SQUIDS

- and SQUID systems, edited by J. Clarke and A. I. Braginski (Wiley-VCH, Weinheim, 2004) Chapter 2, p. 29.
- [31] For the two highest dose values $D = 800$ and 1000 ions/nm, the $j_c(t)$ data shown in Fig. 4 were at $t = 288$ days still far from saturation. Therefore, the values of $j_{c,\infty}$ determined from the fit have huge uncertainties, i.e., one can fit the

experimental data quite well with many combinations of $j_{c,\infty}$ and τ . Therefore, for the two highest doses the $j_{c,\infty}$ values [open symbols in Fig. 5(a)] have been fixed by hand so that they lay exactly on the line shown in Fig. 5(a) (open circles). After fixing $j_{c,\infty}$ for the highest two D values, the parameters b and τ were calculated from the fits of $j_c(t)$.